Journal of Geophysical Research: Space Physics

Key Points:
- Solar wind charge exchanges in magnetosheath produce EUV emissions
- Magnetosheath SWCX EUV emissions change dramatically with solar wind and IMF
- Magnetosheath SWCX EUV emissions can be used to image the global magnetosheath

Correspondence to:
X.-X. Zhang,
xxzhang@cma.gov.cn

EUV emissions from solar wind charge exchange in the Earth's magnetosheath: Three-dimensional global hybrid simulation

Fei He[1], Xiao-Xin Zhang[2], Xue-Yi Wang[3], and Bo Chen[1]

[1]Changchun Institute of Optics, Fine Mechanics and Physics, Chinese Academy of Sciences, Changchun, China, [2]National Center for Space Weather, China Meteorological Administration, Beijing, China, [3]Physics Department, Auburn University, Auburn, Alabama, USA

Abstract In this paper, a three-dimensional (3-D) global hybrid simulation code and a 3-D geocoronal hydrogen model are used to systematically study the extreme ultraviolet (EUV) emissions at 30.4 nm produced by solar wind charge exchange (SWCX) in the Earth's magnetosheath, associated with different solar wind-interplanetary magnetic field (SW-IMF) conditions and different imaging perspectives. We have found that the EUV emission intensities in the magnetosheath are highly variable from several mR to ~1200 mR and increase with the flow speed, the density, the temperature, and the He^{2+}/H^+ density ratio of the solar wind; the northward IMF leads to a minimum emission in the magnetosheath, whereas the southward IMF generates a maximum emission; with the increase of the magnitude of IMF, the emission pattern in the nightside splits from single field-aligned shape into a butterfly shape around the magnetic equator; and the EUV emissions vary with the imaging positions, reflecting different latitudinal and longitudinal information of the magnetosheath. It is noted that the SWCX EUV emissions in the magnetosheath for highly disturbed solar wind conditions should be considered in processing the Moon-based plasmaspheric EUV images. We suggest that EUV imaging of the global magnetosheath requires an EUV imager with large field-of-view, high-sensitivity, large dynamic range, and low intrinsic dark count rate. This investigation could provide us with an overall understanding on SWCX EUV emissions in the magnetosheath which can potentially be used to image the global magnetosheath to study the solar wind-magnetosphere coupling in the future.

1. Introduction

Solar wind charge exchange (SWCX) occurs whenever high-charge state solar wind ions collide with the interstellar neutrals or neutrals in the Earth's geocorona, in which an electron transferring from a neutral to a multiple charged ion is left in an excited state and consequently emits a photon in the extreme ultraviolet (EUV) or soft X-ray (SXR) region when it decays to the ground state [*Paresce et al.*, 1981; *Cravens*, 1997]. In the process of SWCX, high-charge state heavy solar wind ions such as C^{5+}, C^{6+}, N^{7+}, O^{7+}, and O^{8+} can produce SXR emissions [*Lisse et al.*, 2001], while light solar wind ions such as alpha particles (He^{2+} ions) can produce EUV emissions at 30.4 nm [*Paresce et al.*, 1981; *Gruntman*, 1992]. Such SXR and EUV emissions have been observed from a number of comets, planets, interstellar gas in the heliosphere, and even the Moon [*Dennerl et al.*, 1997; *Bhardwaj et al.*, 2002; *Cravens*, 2002; *Wargelin et al.*, 2004; *Krasnopolsky et al.*, 2005; *Ezoe et al.*, 2012, and references therein].

SXR and EUV emissions in the SWCX process take place mainly in the Earth's magnetosheath and vary in different temporal and spatial scales when solar wind impacts the Earth. As the solar wind encounters the dayside magnetosphere, charge exchange between alpha particles and geocoronal hydrogen atoms can produce 30.4 nm emissions in the magnetosheath and even the cusp as well as the nightside ring current regions. SXR and EUV imaging of the magnetosheath can capture the interaction of the solar wind with the magnetosphere. There are many observations and simulation studies on the SWCX SXR emission in the magnetosheath [*Robertson and Cravens*, 2003; *Robertson et al.*, 2006; *Fujimoto et al.*, 2007]. *Gruntman* [1992, 2001] first estimated the diffuse 30.4 nm emission from interplanetary space to be ~1 mR (1 mR = 10^{-3} R and 1 R = $10^6/4\pi$ photons cm^{-2} s^{-1} sr^{-1}), and further calculated the brightness of this emission from the solar wind to be ~3.5 mR at 1 AU from the Sun. These investigations inspire the estimation of the 30.4 nm
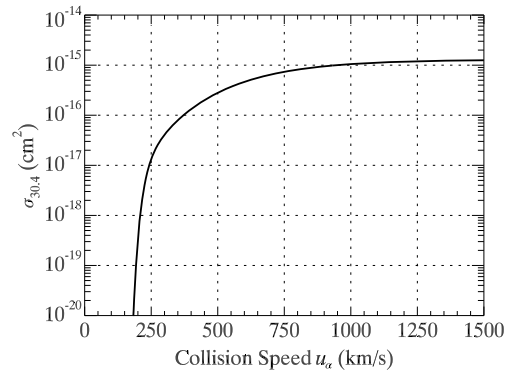
Figure 1. Charge exchange collision cross section for He II 30.4 nm line emission fitted from *Bodewits et al.* [2006].

emission intensity in the magnetosheath to be ~5 mR by *He et al.* [2013] in order to evaluate the noise level contributed by the SWCX EUV emission in the magnetosheath, in which the 30.4 nm emission intensity is below the sensitivity threshold of Chang'e-3 EUV and might have little effect on the Moon-based EUV imaging.

In order to fully understand the 30.4 nm emission characteristics in the process of SWCX in the magnetosphere, the 30.4 nm emission intensity distribution in the magnetosphere will be further investigated in this paper. We will study the variations of the emission intensity with solar wind and interplanetary magnetic field (SW-IMF) conditions from imaging perspectives based on systematical hybrid code simulations of the interaction between solar wind (including alpha particle component) and magnetosphere. In this investigation, the effects of the 30.4 emission in the magnetosheath on the Moon-based EUV imaging and image inversion [*He et al.*, 2011] will be reconsidered, and the potential of imaging the magnetosheath in EUV from the Moon or other orbits in the future will be discussed.

For this purpose, the virtual EUV imager and the simulation configuration involved in *He et al.* [2013] are adopted in the simulation with larger field of view (FOV) of 40° and spatial resolution of 0.2 R_E. The three-dimensional (3-D) global hybrid simulation code and the 3-D geocoronal hydrogen model used in this investigation will be introduced in section 2. The distributions of the EUV emission intensity in the magnetosphere for different SW-IMF conditions from different imaging perspectives will be simulated and discussed in section 3. The summary and conclusion will be given in section 4.

2. Simulation Approach

According to *Gruntman* [1992] and *Robertson and Cravens* [2003], the 30.4 nm emission rate in the SWCX process depends upon the number density of solar wind alpha particles (He^{2+} ions), the solar wind speed, the temperature-dependent collision speed, the collision speed-dependent He^{2+}–H charge exchange cross section [*Bodewits et al.*, 2006; *Gruntman et al.*, 2006], and the number density of geocoronal hydrogen atoms. The plasma parameters and the hydrogen atom density in the magnetosphere are simulated with the 3-D global hybrid simulation code [*Lin et al.*, 2014] and the geocoronal hydrogen model [*Hodges*, 1994], respectively.

2.1. SWCX Emission Calculation

Charge exchange collision between a solar wind alpha particle and a local hydrogen atom produces a proton and an excited singly ionized helium ion:

$$He^{2+} + H \rightarrow He^+(2p) + H^+ \tag{1}$$
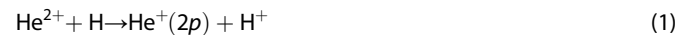
Upon relaxation to ground state He$^+$ (1 s), a 30.4 nm photon is emitted with the emission rate $f(s)$ (photons cm^{-3} s^{-1}) at a given point $s = s(r, \theta, \varphi)$ to be

$$f(s) = f(r, \theta, \varphi) = n_\alpha(r, \theta, \varphi) u_\alpha(r, \theta, \varphi) n_H(r, \theta, \varphi) \sigma_{30.4}(u_\alpha) \tag{2}$$

where n_α is the alpha particle number density in the magnetosheath, u_α is the collision speed between solar wind alpha particles and local hydrogen atoms, n_H is the number density of local hydrogen atoms, $\sigma_{30.4}(u_\alpha)$ is the collision speed-dependent cross section to produce a 30.4 nm photon, and (r, θ, φ) are the geocentric distance, latitude and longitude in the geocentric solar magnetospheric (GSM) coordinate system, respectively. Normally, the speed of the hydrogen atoms in geocorona is much slower than that of the upstream solar wind flow, and u_α is very close to the solar wind speed V_{sw}. In the magnetosheath region, however, most of the bulk kinetic energy of the solar wind flow has been
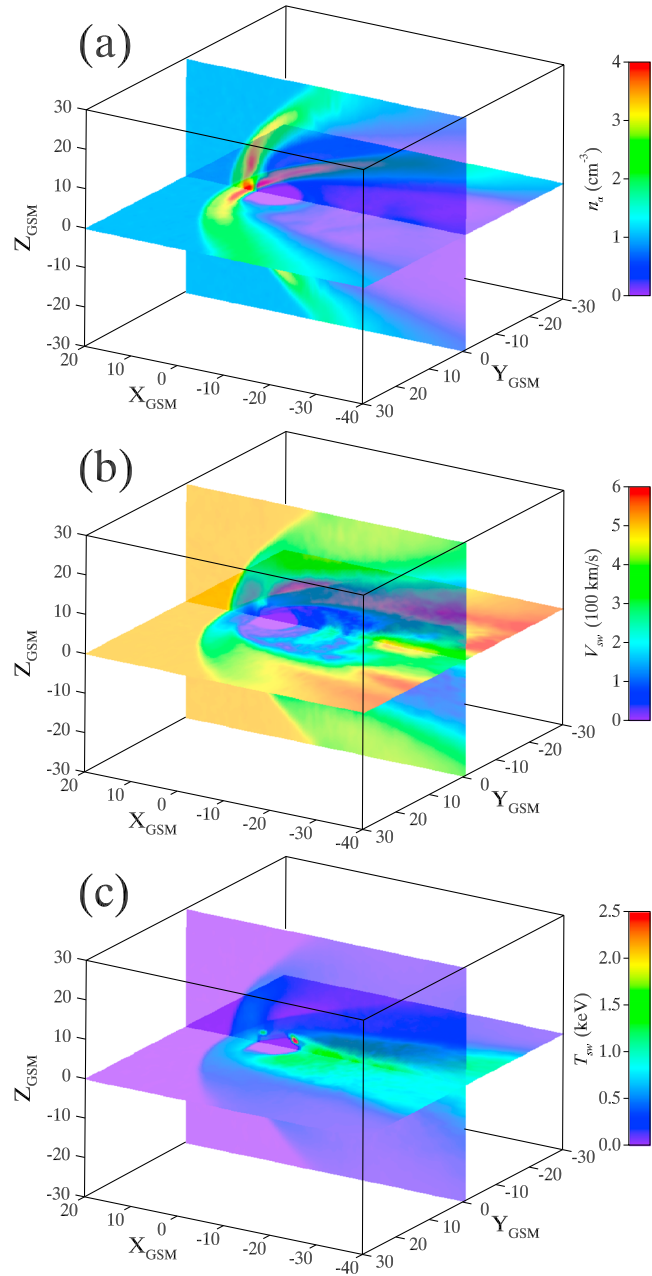
Figure 2. Cut views of the hybrid simulation results of (a) n_α, (b) V_{sw}, and (c) T_{sw} in GSM coordinate system with corresponding color bars shown at the right, respectively. The SW-IMF parameters driving the hybrid model are $V_{sw} = 500 \, \text{km s}^{-1}$, $N_{sw} = 10 \, \text{cm}^{-3}$, $T_{sw} = 20 \, \text{eV}$, $B_T = 10 \, \text{nT}$, $\theta_c = 180°$ (B_T and θ_c are defined in section 3), and $f_\alpha = 0.1$.

converted to thermal energy, and the thermal speed V_{th} becomes an important contributor to u_α [*Robertson et al.*, 2006]. The thermal speed is calculated by

$$V_{th} = \sqrt{\frac{3k_B T_{sw}}{m_p}} \qquad (3)$$

where k_B is the Boltzmann constant, T_{sw} is the temperature of the solar wind, and m_p is the mass of a solar wind proton. Then, the collision speed is given by the averaged total ion speed as follows:
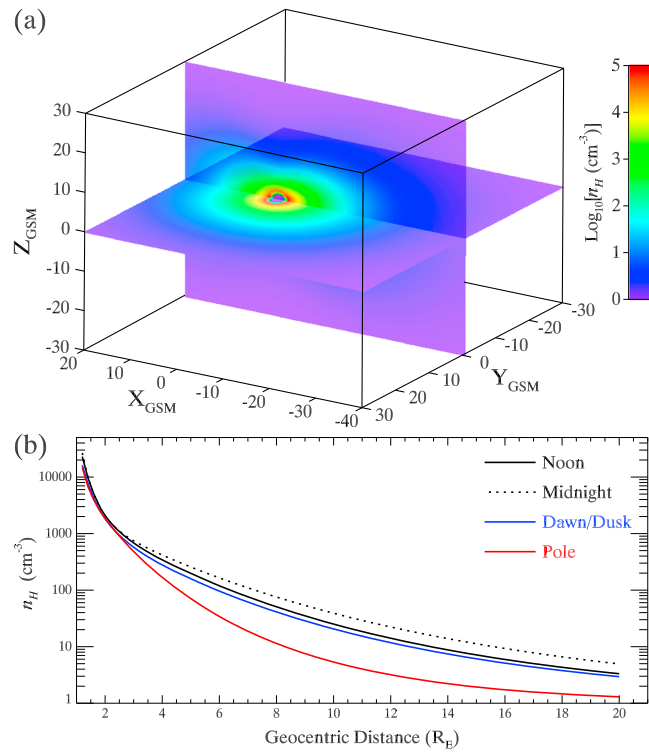
$$u_\alpha = \sqrt{V_{sw}^2 + V_{th}^2} \qquad (4)$$

Figure 3. (a) Cutoff views of n_H and (b) geocentric distance dependences of n_H in directions toward the Sun (black solid), the midnight (black dashed), the dawn/dusk (blue solid), and the North/South Pole (red solid).
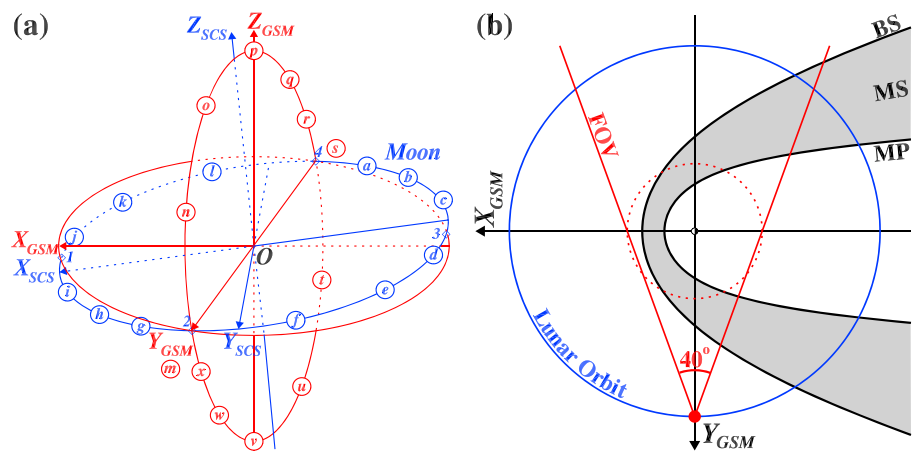

Figure 4. (a) The SCS and GSM coordinate systems used in this investigation and (b) FOV of the virtual imager projected onto GSM equatorial plane. The blue ellipses approximately represent the lunar orbit plane. The four diamonds in Figure 4a represent the lunar phases with the first for the new Moon, the second for the first-quarter Moon, the third for the full Moon, and the fourth for the last-quarter Moon. Position m is used in sections 3.1–3.3 while the positions $a–l$ (blue circles) and $m–x$ (red circles) are used in section 3.4. Positions m and s are actually at the second and the fourth diamonds, respectively. BS, MP, and MS in panel Figure 4b are bow shock, magnetopause (thick black curves) and magnetosheath (gray region), respectively. In Figure 4b, the two red solid lines define the FOV of 40°, and the red dashed circle represents the projection of the FOV on the GSM equator plane from the North Pole 60 R_E away from the Earth's center.

Table 1. SW-IMF Parameters Used in the Simulations[a]

Category	B_T (nT)	θ_c (°)	V_{sw} (km s^{-1})	N_{sw} (cm^{-3})	T_{sw} (eV)	f_α	Position
I	10	$-180 \sim 180 \vert 45$	500	10	20	0.10	m
II	$6 \sim 38 \vert 4$	180	500	10	20	0.10	m
III	10	180	$300 \sim 800 \vert 100$	10	20	0.10	m
IV	10	180	500	$5 \sim 40 \vert 7$	20	0.10	m
V	10	180	500	10	$5 \sim 45 \vert 8$	0.10	m
VI	10	180	500	10	20	$.05 \sim .3 \vert .05$	m
VII	25	180	700	40	50	0.20	$a - x$

[a]Note that the values before and after "|" refer to the ranges and steps of the parameters, respectively.
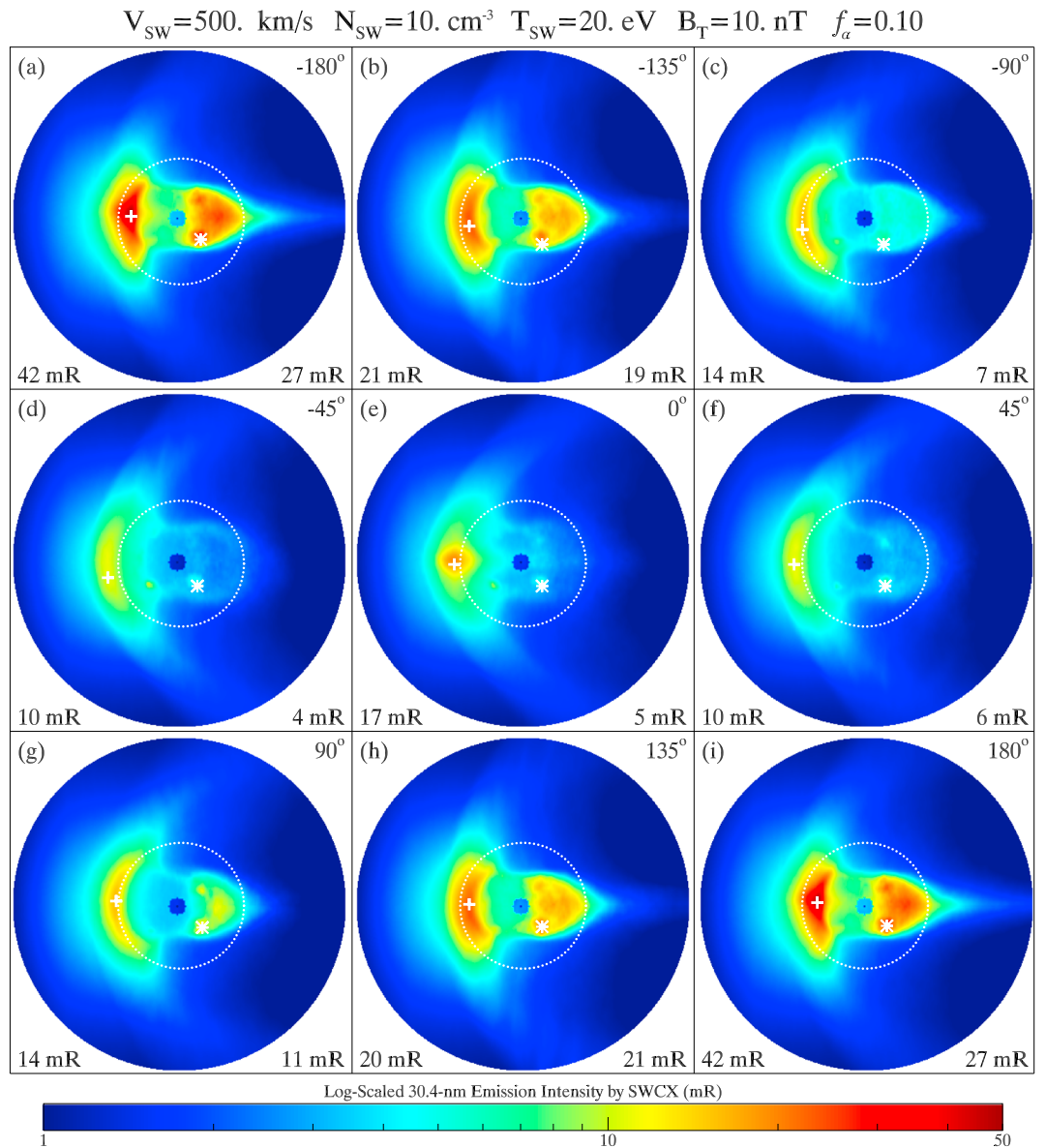

Figure 5. SWCX emission intensity for θ_c from $-180°$ to $180°$ at $45°$ steps at position m. Note that the IMF clock angle, the dayside maximum emission intensity (indicated by the white crosses) and the nightside maximum intensity (indicated by the white stars) are shown in the upper right, the lower left and the lower right corners of each box. All the other fixed parameters are shown at the top. The dotted circle in each box represents a FOV of $15°$. The images are projected in the GSM xz plane with the $+X_{GSM}$ axis to the left and the $+Z_{GSM}$ axis to the up. The log-scaled color bar is shown at the bottom.
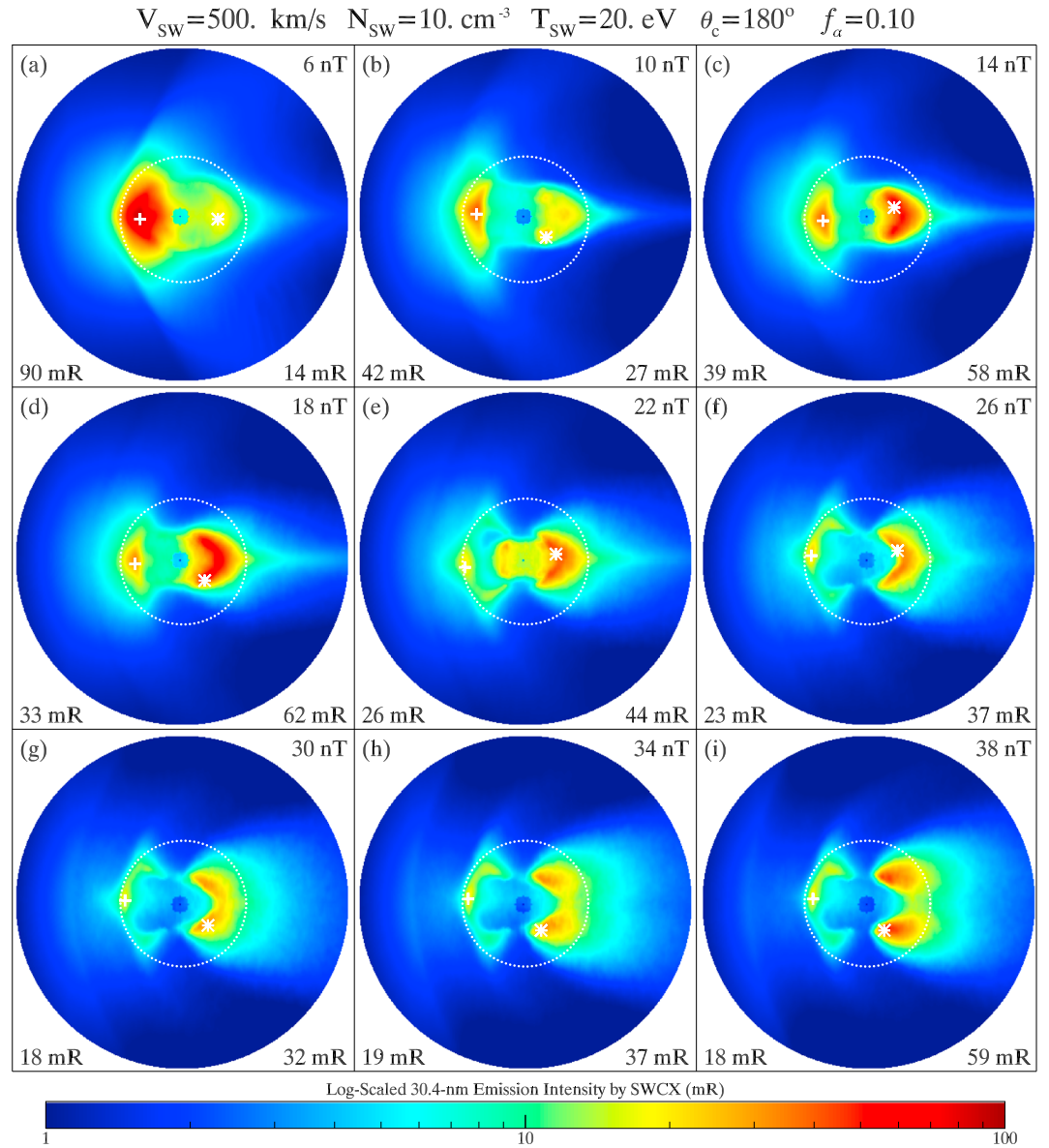
$V_{SW}=500. \text{ km/s} \quad N_{SW}=10. \text{ cm}^{-3} \quad T_{SW}=20. \text{ eV} \quad \theta_c=180° \quad f_\alpha=0.10$

Log-Scaled 30.4-nm Emission Intensity by SWCX (mR)

Figure 6. Dependence of SWCX emission intensity on B_T which is increased from 6 nT to 38 nT for every 4 nT as noted in the upper right of each box. All the other settings are the same as those in Figure 5.

For convenience of calculations in the simulation, we have fitted the collision cross section curve in *Bodewits et al.* [2006] to the following form:

$$\sigma_{30.4}(u_\alpha) = 10^{-14.89-4.90\exp(-u_\alpha/249.84)-4270.64\exp(-u_\alpha/24.91)} \quad (5)$$

The cross section calculated by above formula has considered the additional contribution from the He$^+$ (2 s) state [*Bodewits et al.*, 2006]. The variation of $\sigma_{30.4}$ versus u_α is shown in Figure 1. When u_α increases from ~250 km s^{-1} to ~750 km s^{-1}, $\sigma_{30.4}$ is increased by 2 orders of magnitude but varies not much for $u_\alpha > 750$ km s^{-1}.

The 30.4 nm emission intensity I (photons cm^{-2} s^{-1} sr^{-1}) at an observation point is given by the integration of $f(s)$ along a line of sight (LOS):

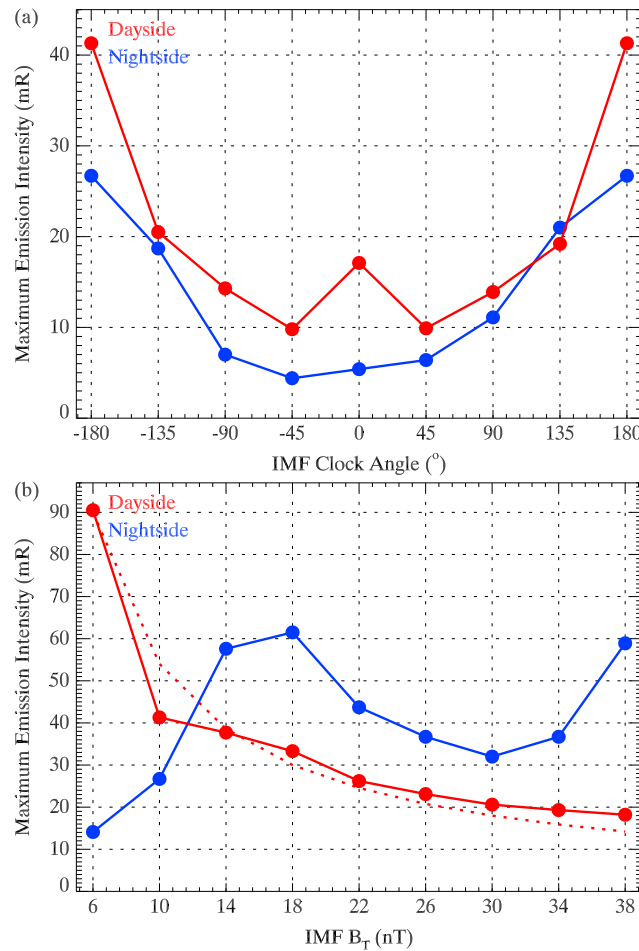$$I = \frac{1}{4\pi} \int_{LOS}^{\infty} f(s)ds, \quad (6)$$

Figure 7. The maximum emission intensity as a function of (a) θ_c with all other inputs fixed with $V_{sw} = 500$ km/s, $N_{sw} = 10$ cm^{-3}, $T_{sw} = 20$ eV, $B_T = 10$ nT, and $f_\alpha = 0.1$ and (b) B_T with all other inputs fixed with $V_{sw} = 00$ km/s, $N_{sw} = 10$ cm^{-3}, $T_{sw} = 20$ eV, $\theta_c = 180°$, and $f_\alpha = 0.1$. The red dashed line in Figure 7b is the fitting of the red points to $1/B_T$.

The main task in equation (6) is to determine n_α, u_α, and n_H, for which the simulation approaches will be described below.

2.2. Calculation of n_α and u_α

The solar wind alpha particle number density, the solar wind speed, and the solar wind temperature in the magnetosheath can be obtained through a 3-D global hybrid simulation code [*Lin et al.*, 2014], which extends the previous version of the code that contains only the dayside magnetosphere [*Swift*, 1996; *Lin and Wang*, 2005] to include the nightside. In the hybrid code the ions (protons and alpha particles) are treated as discrete particles, while the electrons are treated as a massless fluid. Quasi charge neutrality is assumed in the simulation. The equation for ion particle motion in the simulation units is given as

$$\frac{d\mathbf{v}_p}{dt} = \mathbf{E} + \mathbf{v}_p \times \mathbf{B} - \nu(\mathbf{V}_p - \mathbf{V}_e) \quad (7)$$

where $\mathbf{v}_p$ is the ion particle velocity, $\mathbf{E}$ is the electric field, $\mathbf{B}$ is the magnetic field, ν is an ad hoc current-dependent collision frequency with a typical value of $\sim 10^{-4}\Omega_i$ (ion gyrofrequency) but with typical peak of ~ 0.01–$0.1\Omega_i$ [*Tan et al.*, 2011] near the magnetopause, and $\mathbf{V}_e$ and $\mathbf{V}_p$ are the bulk flow velocities of electrons and ion

particles, respectively. The collision term in equation (7) is only applied to the dayside magnetopause to trigger the reconnections for southward IMF and the simulation results are not sensitivity to it. In addition to the particle ions, a cold, incompressible ion fluid is assumed to be dominant in the inner magnetosphere, acting as an role for flow of field-aligned currents and propagation of Alfvén waves between the magnetosphere and the ionospheric shell near the Earth [*Swift*, 1996; *Raeder*, 2003; *Lin and Wang*, 2005; *Omidi et al.*, 2005], since the dynamics and ion kinetic physics are considered in the outer magnetosphere ($r > 6.5$ R_E) in our simulation. The number density of the cold ion fluid in the region of $r \leq 6.5$ R_E is [*Lin et al.*, 2014]

$$N_f = (N_{eq}/r^3)[1 - \tanh(r - 6.5)] \quad (8)$$

where r is the geocentric distance in unit of R_E, and $N_{eq} = 1000$ cm^{-3}.

A massively parallel computation is performed. In the simulation, the solar wind flows along the $-x$ direction from the frontside boundary at $r = 20$ R_E. Nonuniform cell grids of $(\Delta x, \Delta y, \Delta z) = (0.2$ R_E, 0.2 R_E, 0.2 $R_E)$, $(0.12$ R_E, 0.2 R_E, 0.2 $R_E)$, and $(0.4$ R_E, 0.4 R_E, 0.4 $R_E)$ are adopted in the near-Earth regions with $x \geq -20$ R_E, -12 $R_E \leq y \leq 12$ R_E, and -12 $R_E \leq z \leq 12$ R_E, around the bow shock, magnetosheath, and magnetopause, and in the lobes, respectively. The bow shock, magnetosheath, and magnetopause are formed from the interaction between the superfast solar wind and the geomagnetic field (dipole field with tilt angle equals to zero).
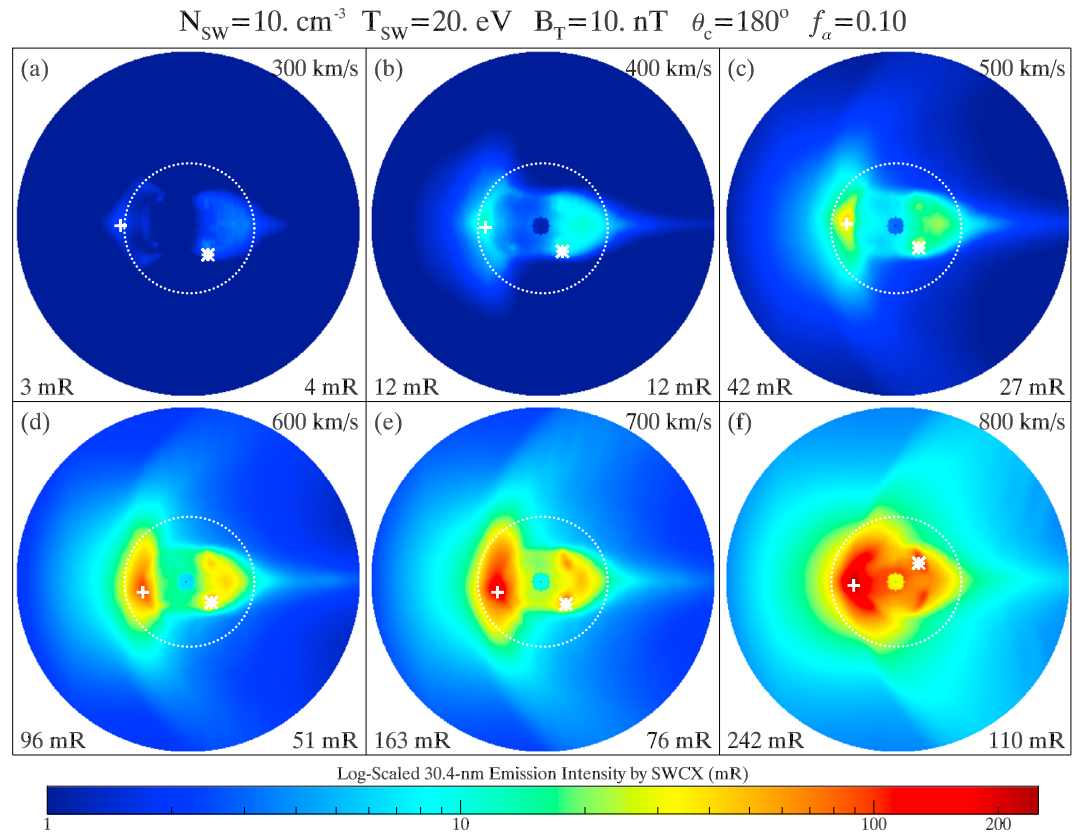
Figure 8. Dependence of SWCX emission intensity on V_{sw} which is increased from 300 km s^{-1} to 800 km s^{-1} for every 100 km s^{-1} as noted in the upper right corner of each box. All the other settings are the same as those in Figure 5.

The input parameters of the hybrid simulation code include solar wind speed V_{sw}, solar wind number density N_{sw}, solar wind temperature T_{sw}, IMF components B_x, B_y, and B_z in GSM coordinate system and the He^{2+}/H$^+$ density ratio f_α in the solar wind. The configurations of the magnetosheath in different SW-IMF conditions can be obtained by using this hybrid simulation code. The maximum uncertainty of the ion flux in the hybrid simulation is approximately $1/\sqrt{N_{cell}}$ (N_{cell} is the average particle number per cell of about 150–400).

As an example, Figures 2 presents the cutoff views of the distributions of n_α, V_{sw}, T_{sw} on different planes in GSM for moderate SW-IMF conditions. All the three parameters output from the hybrid model are in the spatial scope of $-40\,R_E \leq x \leq 20\,R_E$, $-30\,R_E \leq y \leq 30\,R_E$, and $-30\,R_E \leq z \leq 30\,R_E$ with a uniform grid size of $(\Delta x, \Delta y, \Delta z) = (0.2\,R_E, 0.2\,R_E, 0.2\,R_E)$. Structures of bow shock, magnetosheath, and magnetopause are clearly shown, and the cusp region can also be seen though not so significantly in Figure 2. The model results are put into equations (2)–(6) to get the 30.4 nm emission intensity in the SWCX process in the magnetosheath at different imaging perspectives.

2.3. Calculation of n_H

In calculation of the number density of geocoronal hydrogen atoms, the Monte Carlo model of *Hodges* [1994] is adopted. This model is global and three-dimensional compared with other models [*Rairden et al.*, 1986; *Tinsley et al.*, 1986; *Bishop*, 1999; *Østgaard et al.*, 2003; *Bailey and Gruntman*, 2011; *Fuselier et al.*, 2010] and has included both the neutral-neutral and the ion-neutral interaction processes and examined seasonal and solar cycle effects on the exospheric density, so it is suitable for calculations in this paper. The number density of hydrogen atoms at a position (r, θ, φ) is calculated by

$$n_H(r, \theta, \phi) = N(r)\sqrt{4\pi}\sum_{l=0}^{3}\sum_{m=0}^{l}\{A_{lm}\cos(m\phi) + B_{lm}\sin(m\phi)\}Y_{lm}(\theta) \qquad (9)$$

where the altitude-dependent parameters $N(r)$, A_{lm}, and B_{lm} are given in *Hodges* [1994] (also available from NASA-Community Coordinated Modeling Center (CMCC)), and $Y_{lm}(\theta)$ is the spherical harmonic
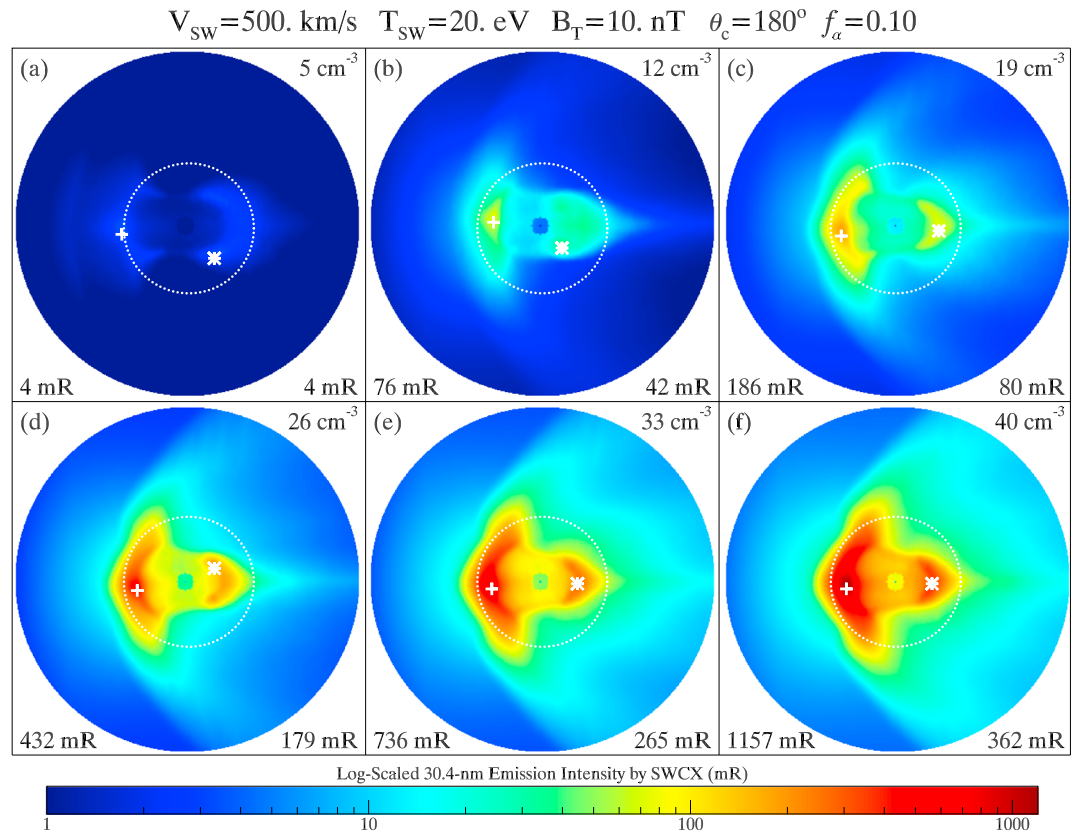
$V_{SW}=500.$ km/s $T_{SW}=20.$ eV $B_T=10.$ nT $\theta_c=180°$ $f_\alpha=0.10$

Figure 9. Dependence of SWCX emission intensity on N_{sw} which is increased from 5 cm^{-3} to 40 cm^{-3} for every 7 cm^{-3} as noted in the upper right corner of each box. All the other settings are the same as those in Figure 5.

Legendre function. Beyond 12 R_E, the outer boundary of the model, a 1/r^3 radial variation is usually used to extrapolate the model [*Robertson and Cravens*, 2003; *Robertson et al.*, 2006], which may make the density decreases too fast [*Østgaard et al.*, 2003; *Bailey and Gruntman*, 2011]. Here an exponential decay function of the form $n_H = A_0\exp(-r/t_1) + A_1\exp(-r/t_2)$ is adopted to extrapolate the *Hodges* [1994] model, in consistent with *Østgaard et al.* [2003] and *Bailey and Gruntman* [2011]. The calculations of the exosphere are all performed at equinox for $F_{10.7} = 230$ corresponding to solar maximum in this investigation. Figure 3 shows the cutoff views and the geocentric distance dependences of n_H associated with a significant day-night asymmetry, and n_H at 8 R_E at equator noon is ~40 cm^{-3} in consistent with the result of *Bailey and Gruntman* [2011] and is slightly larger than that of *Fuselier et al.* [2010].

3. Dependence of Intensity on Various Parameters

In this section we use the models described in the previous section to study the 30.4 nm emission intensity in the SWCX process in the magnetosheath under different SW-IMF conditions at different observation positions. Twelve points represented by the blue circles in the lunar orbit in Figure 4 are selected to investigate the emission intensity distributions from different lunar phases and the coordinates of these points are all in GSM in units of R_E. Three points are selected during adjacent lunar phases. The points located in the first-quarter Moon to the full Moon sector of the lunar orbit are marked with *d*: (−51.4, 21.9, 11.9), *e*: (−39.9, 40.8, 9.0), and *f*: (−22.0, 54.3, 4.8), and the points located in the full Moon to the last-quarter Moon sector of the lunar orbit are marked with *a*: (−21.8, −54.3, 5.5), *b*: (−39.7, −40.8, 9.5), and *c*: (−51.3, −21.9, 12.2). The remaining six points *g*–*l* are symmetric to above points with respect to the Y_{GSM} axis. The dipole tilt angle is not considered in this study, so the positions are identical with those in *He et al.* [2013], suitable for comparisons between plasmaspheric emission and magnetosheath emission. Another 12 points *m*–*x* marked by the red circles in a virtual polar circular orbit (PCO) with a radius of 60 R_E in the
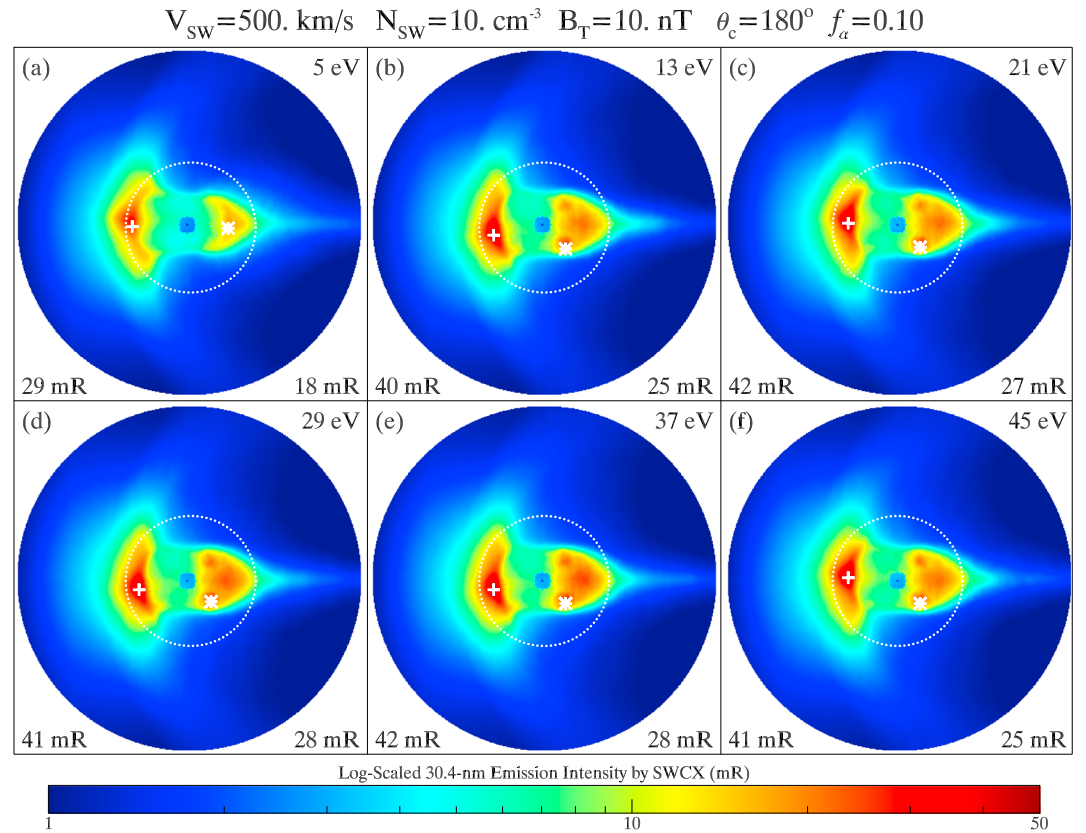
$V_{SW}=500.$ km/s $N_{SW}=10.$ cm^{-3} $B_T=10.$ nT $\theta_c=180^{\circ}$ $f_a=0.10$

Figure 10. Dependence of SWCX emission intensity on T_{sw} which is increased from 5 eV to 45 eV for every 8 eV as noted in the upper right corner of each box. All the other settings are the same as those in Figure 5.

GSMyz plane are also used in the simulations to further investigate the emission intensity at different perspectives. All simulated EUV images are projected in the yz plane in the satellite coordinate system (SCS) as defined in Figure 4. The X_{SCS} axis is along the axis of the FOV of the imager and the other axes are determined by rotating of corresponding GSM axes to form a right-handed orthogonal system, with Z_{SCS} axis always pointing to the north. In all the simulated EUV images below, the axes are in units of R_E, the spatial scope is between $-20\,R_E$ and $20\,R_E$ for both axes with the Earth at center, and the spatial resolution is $0.2\,R_E \times 0.2\,R_E$, sufficiently high for the large scale structures to be evident.

In order to simulate the 30.4 nm emission of the magnetosheath under different SW-IMF conditions, the seven categories of simulations listed in Table 1 are adopted in this study. The variables for each category include V_{sw}, N_{sw}, T_{sw}, IMF B_T, IMF clock angle θ_c, and f_a. IMF B_T is defined as $B_T = \sqrt{B_y^2 + B_z^2}$ ($B_x = 0.5$ nT, not used in our simulation). The IMF clock angle, $\theta_c = a\tan(B_y/B_z)$, is defined as the angle, looking to the Earth from the Sun, clockwise/anticlockwise (positive/negative) from the z axis in the GSM yz plane. From categories I to VI, only one parameter is variable from low to high values for each category and other parameters are fixed to their average levels, and the imaging position is fixed at position m (0.0, 60.0 R_E, 0.0) in Figure 4. In category VII, all parameters are setup to a highly disturbed SW-IMF condition for all imaging positions in Figure 4 in order to give us a general understanding on the distributions of the emission intensity at different perspectives.

3.1. Dependence of Emissions on IMF

Magnetosheath EUV emission intensities simulated for θ_c increasing from $-180°$ to $180°$ at $45°$ steps are shown in Figure 5 (category I) and the corresponding maximum emission intensities in dayside (red) and nightside (blue) are plotted in Figure 7a. All other inputs are fixed with $V_{sw} = 500$ km/s, $N_{sw} = 10$ cm^{-3},
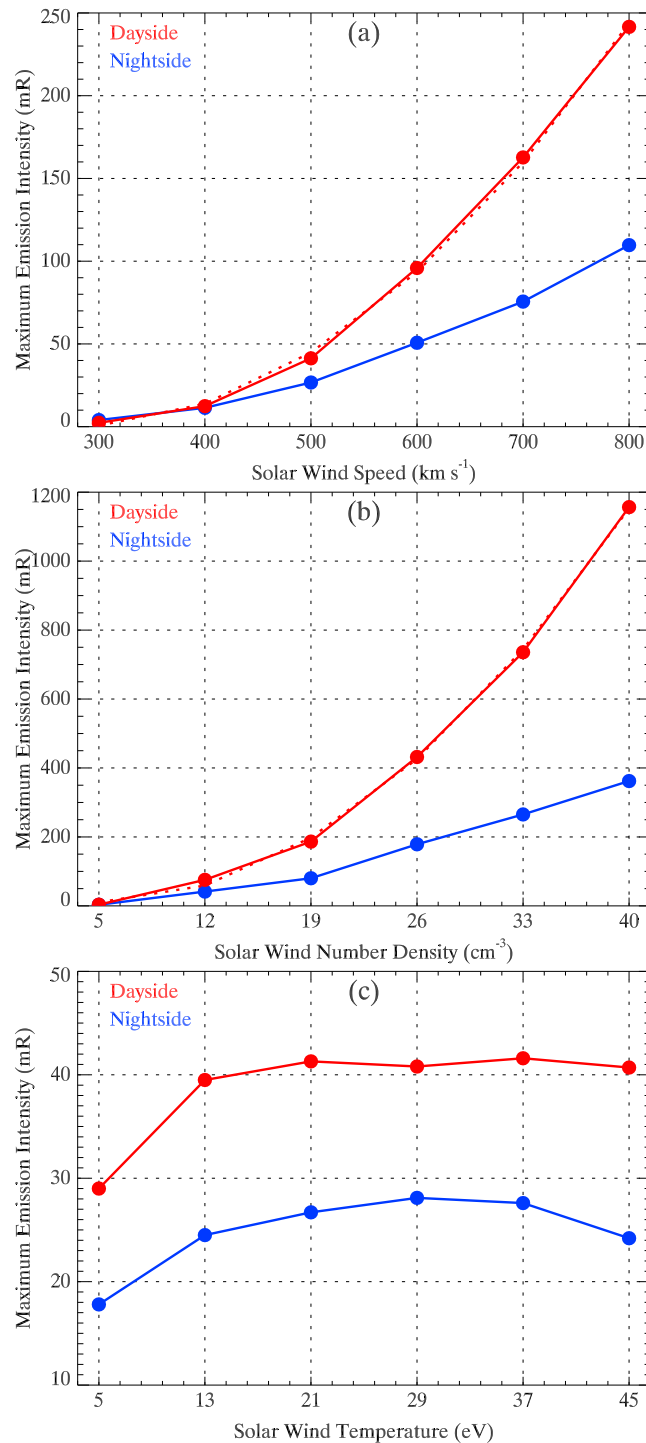
Figure 11. The maximum emission intensity as a function of (a) V_{sw} with all other inputs fixed with $N_{sw} = 10$ cm^{-3}, $T_{sw} = 20$ eV, $B_T = 10$ nT, $\theta_c = 180°$, and $f_\alpha = 0.1$, (b) N_{sw} with all other inputs fixed with $V_{sw} = 500$ km/s, $T_{sw} = 20$ eV, $B_T = 10$ nT, $\theta_c = 180°$, and $f_\alpha = 0.1$, and (c) T_{sw} with all other inputs fixed with $V_{sw} = 500$ km/s, $N_{sw} = 10$ cm^{-3}, $B_T = 10$ nT, $\theta_c = 180°$, and $f_\alpha = 0.1$. The dashed lines in Figures 11a and 11b represent the best fit to quadratic polynomial.

$T_{sw} = 20$ eV, $B_T = 10$ nT, and $f_\alpha = 0.1$. It is clearly revealed in Figure 5 that θ_c controls EUV emission intensity patterns in the magnetosheath. Increasing $|\theta_c|$ results in enhancements of the EUV emissions in both dayside and nightside in the magnetosphere. Positive and negative θ_c with the same magnitudes, such as 45° and −45°, produce approximately the same emission distributions as shown in Figures 5d, 5f, and 7a. Northward IMF ($\theta_c = 0°$) leads to a minimum EUV emission, whereas southward IMF ($\theta_c = 180°$) generates a maximum EUV emission. The more southward the IMF is, the larger the emission intensity is. As the IMF turns from northward to southward, the magnetic reconnection at magnetopause becomes more and more apparent [*Bothmer and Daglis*, 2007], allowing the magnetosheath plasma to transfer into polar cusp region where the alpha particles are trapped by Earth's magnetic field lines and piled up in the nightside ring current region. Therefore, as $|\theta_c|$ increases, the cusp region becomes apparent and the nightside emission intensity increases as demonstrated by Figure 5.

Figures 6 shows the magnetosheath EUV emission intensities for B_T increasing from 6 nT to 38 nT at 4 nT steps for a fixed IMF clock angle of 180° (category II) and the corresponding maximum emission intensities in dayside (red) and nightside (blue) are plotted in Figure 7b. All other inputs are fixed with $V_{sw} = 500$ km/s, $N_{sw} = 10$ cm^{-3}, $T_{sw} = 20$ eV, $\theta_c = 180°$, and $f_\alpha = 0.1$. With the increase of B_T, the dayside maximum emission intensity decreases with emission pattern expanding to cusp region, whereas the nightside maximum emission intensity changes up and down with emission patterns splitting from single field-aligned shape into a butterfly shape around the magnetic equator. The red dashed line in Figure 7b represents the fitting of the
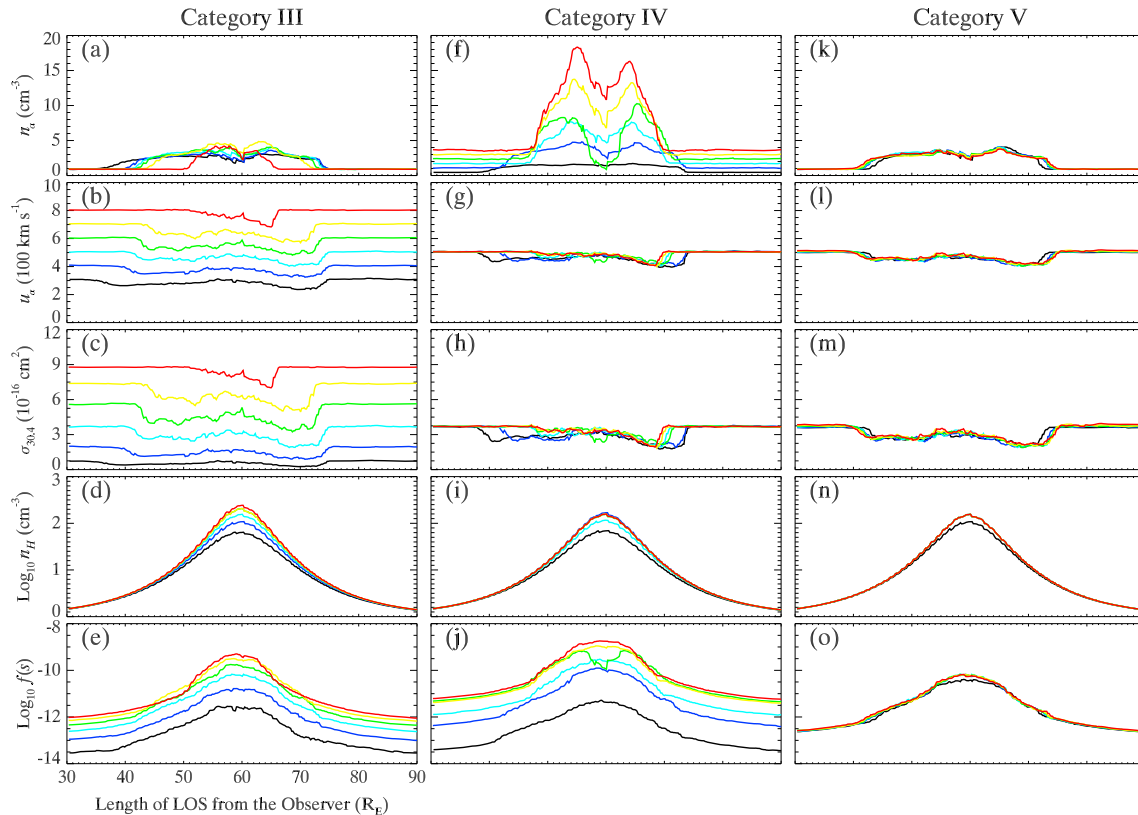
Figure 12. Dayside plasma parameters in the magnetosheath along the LOS with the maximum emission intensity. Categories (a–e) III, (f–j) IV, and (k–o) V, respectively. The parameters are n_α in Figures 12a, 12f, and 12k, u_α in Figures 12b, 12g, and 12l, $\sigma_{30.4}$ in Figures 12c, 12h, and 12m, n_H in Figures 12d, 12i, and 12n, and $f(s)$ in Figures 12e, 12j, and 12o, respectively. The color lines with the sequence *black, blue, cyan, green, yellow,* and *red* represent the six cases for each category, respectively, with *black* for the lowest value and *red* for the highest value of the variable of each category.

red points to a function proportional to $1/B_T$. It can be inferred that increasing of B_T results in decreases of both Alfvén Mach number MA and magnetosonic Mach number M_{ms}, and in turn weakens the compression of the magnetosheath, leading to the decrease of emission intensity in the magnetosheath.

It can be seen that, in the intensity images there are SWCX emissions from the nightside and cusp regions especially for southward IMF (Figures 5a, 5b, and 5h–5i), but with relatively low intensity compared with dayside. The ions enter the inner magnetosphere through dayside magnetopause reconnection and nightside tail reconnection, as well as though the cusp penetration. These trapped ions drift under the magnetic gradient and curvature forces in the inner magnetosphere and are convected to the near-nightside to enhance the ion density in the ring current region [*Lin et al.*, 2014]. Detailed studies on the ion dynamics in these regions will be conducted in future investigation.

3.2. Dependence of Emissions on V_{sw}, N_{sw}, and T_{sw}

Figures 8 and 11a show the magnetosheath EUV emission intensity distributions and the maximum emission intensities, respectively, with V_{sw} increasing from $300\,\mathrm{km\,s^{-1}}$ to $800\,\mathrm{km\,s^{-1}}$ at $100\,\mathrm{km\,s^{-1}}$ steps (category III) with all other parameters fixed with $N_{sw} = 10\,\mathrm{cm^{-3}}$, $T_{sw} = 20\,\mathrm{eV}$, $B_T = 10\,\mathrm{nT}$, $\theta_c = 180°$, and $f_\alpha = 0.1$, Figures 9 and 11b show the dependences of the magnetosheath EUV emission intensity distributions and the maximum emission intensities, respectively, on different N_{sw} increasing from 5 to $40\,\mathrm{cm^{-3}}$ at $7\,\mathrm{cm^{-3}}$ steps (category IV) with all other parameters fixed with $V_{sw} = 500\,\mathrm{km/s}$, $T_{sw} = 20\,\mathrm{eV}$, $B_T = 10\,\mathrm{nT}$, $\theta_c = 180°$, and $f_\alpha = 0.1$, and Figures 10 and 11c show the variations of the magnetosheath EUV emission intensity distributions and the maximum emission intensities, respectively, with T_{sw} increasing from 5 to $45\,\mathrm{eV}$ at $8\,\mathrm{eV}$ steps (category V) with all other parameters fixed with $V_{sw} = 500\,\mathrm{km/s}$, $N_{sw} = 10\,\mathrm{cm^{-3}}$, $B_T = 10\,\mathrm{nT}$, $\theta_c = 180°$, and $f_\alpha = 0.1$. The LOS information corresponding to the dayside maxima in Figure 11 are plotted in Figure 12.
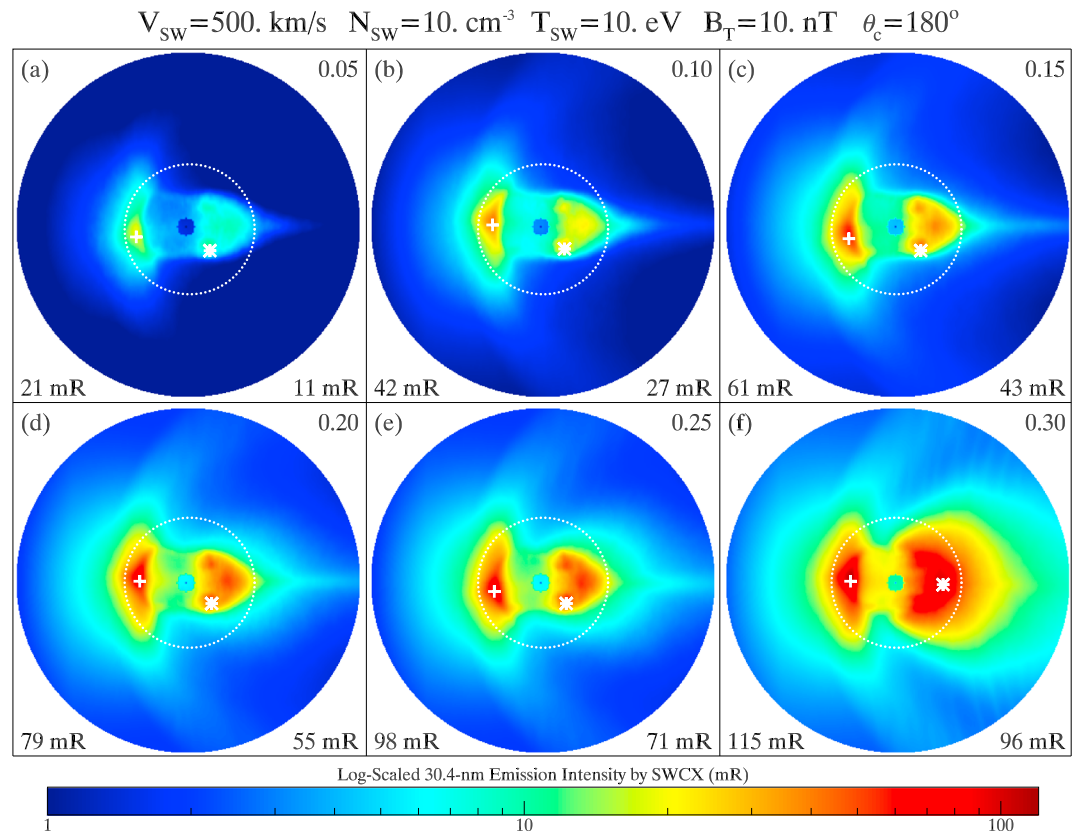
$V_{sw} = 500.\ \text{km/s}\quad N_{sw} = 10.\ \text{cm}^{-3}\quad T_{sw} = 10.\ \text{eV}\quad B_T = 10.\ \text{nT}\quad \theta_c = 180^\circ$

Log-Scaled 30.4-nm Emission Intensity by SWCX (mR)

Figure 13. Dependence of SWCX emission intensity on f_α which is increased from 0.05 to 0.3 for every 0.05 as noted in the upper right corner of each box. All the other settings are the same as those in Figure 5.

Figures 8, 9, 11a and 11b demonstrate that the SWCX EUV emissions in the magnetosheath quadratically increase with both V_{sw} and N_{sw}, respectively, with the emission region apparently approaching the Earth. It can be seen in Figures 12a–12j that the intensification of SWCX EUV emissions with V_{sw} is mainly due to the enhancements in u_α and $\sigma_{30.4}$, and with N_{sw} is mainly caused by the enhancement in n_α, respectively, based on the fact that an increase in solar wind dynamic pressure $P_d = N_{sw}V_{sw}^2$ compresses the magnetosheath close to the Earth [*Shue et al.*, 1998; *Chao et al.*, 2002; *Lin et al.*, 2010], allowing more solar wind alpha particles to enter the magnetosheath and other regions (such as the dayside geosynchronous orbit region, the cusp region, and the nightside ring current region) where n_H is higher. Figures 10, 11c, and 12k–12o reveal that the dayside emissions have an obvious increase with T_{sw} increasing from 5 eV to 13 eV due to the increase of n_H and do no change much when $T_{sw} > 13$ eV, whereas the nightside emissions increase with T_{sw} increasing from 5 eV to 29 eV and then decrease when $T_{sw} > 29$ eV.

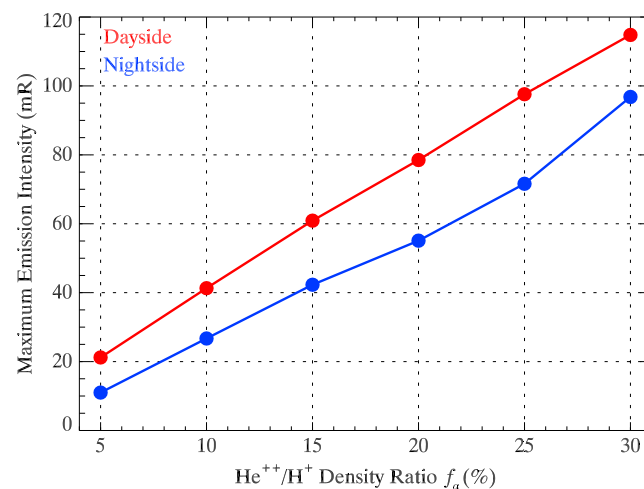**Figure 14.** The maximum emission intensity as a function of f_α with all other inputs fixed with $V_{sw} = 500$ km/s, $N_{sw} = 10$ cm^{-3}, $T_{sw} = 20$ eV, $B_T = 10$ nT, $\theta_c = 180°$, and $f_\alpha = 0.1$.
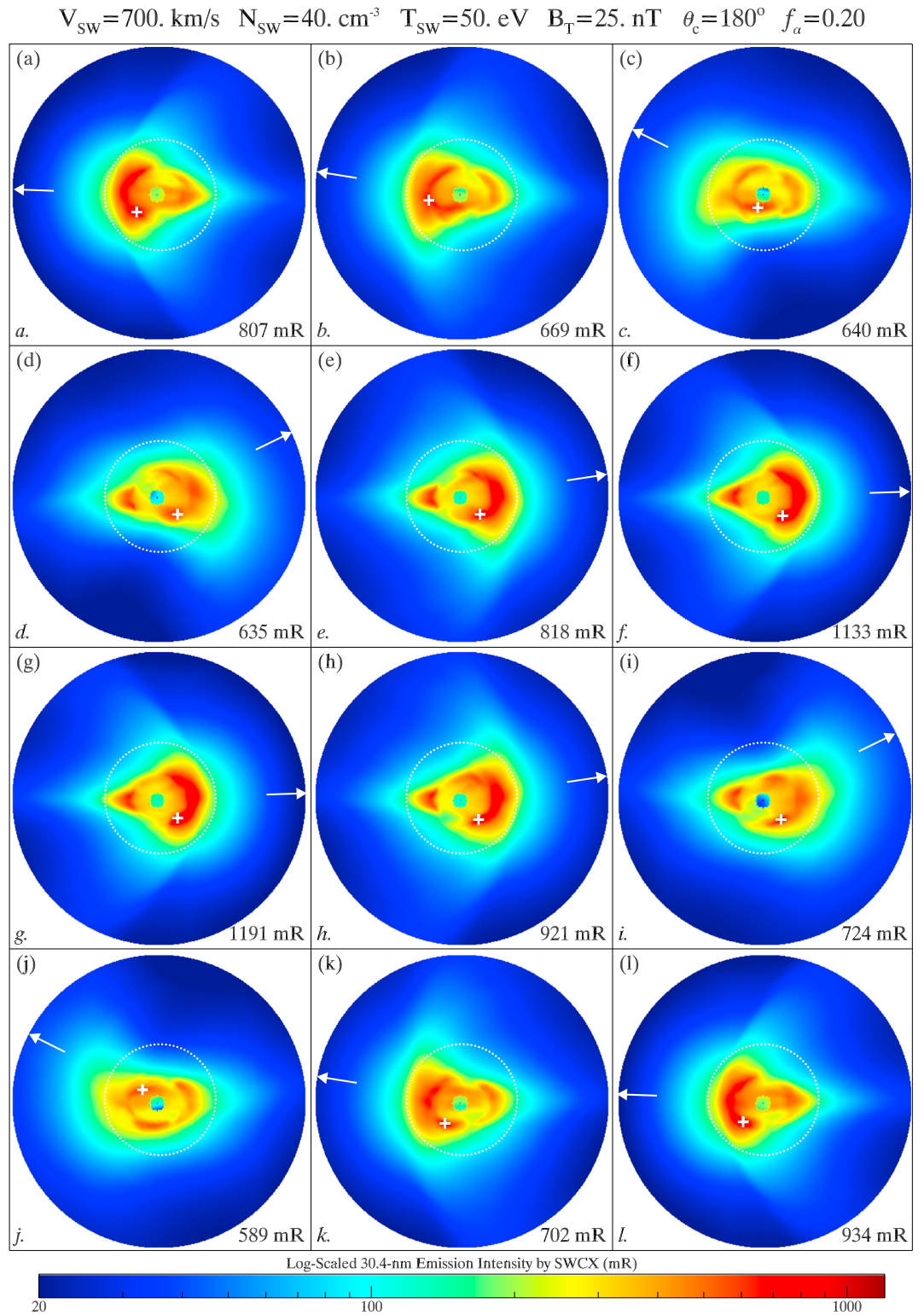
Figure 15. Magnetosheath EUV emission intensity simulated at the 12 lunar positions in Figure 4. Each box represents a lunar position in Figure 4 as indicated at the lower left corner of each box. The projection plane for all the boxes are in the SCS yz plane, the Y_{SCS} axis is in horizontal direction with positive to the right and the Z_{SCS} axis is along the vertical direction with positive to the up. The white arrows in each box indicate the projection of the X_{GSM} axis in the image plane, respectively. All the other settings are the same as those in Figure 5.

$V_{SW}=700.\ km/s\quad N_{SW}=40.\ cm^{-3}\quad T_{SW}=50.\ eV\quad B_T=25.\ nT\quad \theta_c=180^o\quad f_\alpha=0.20$

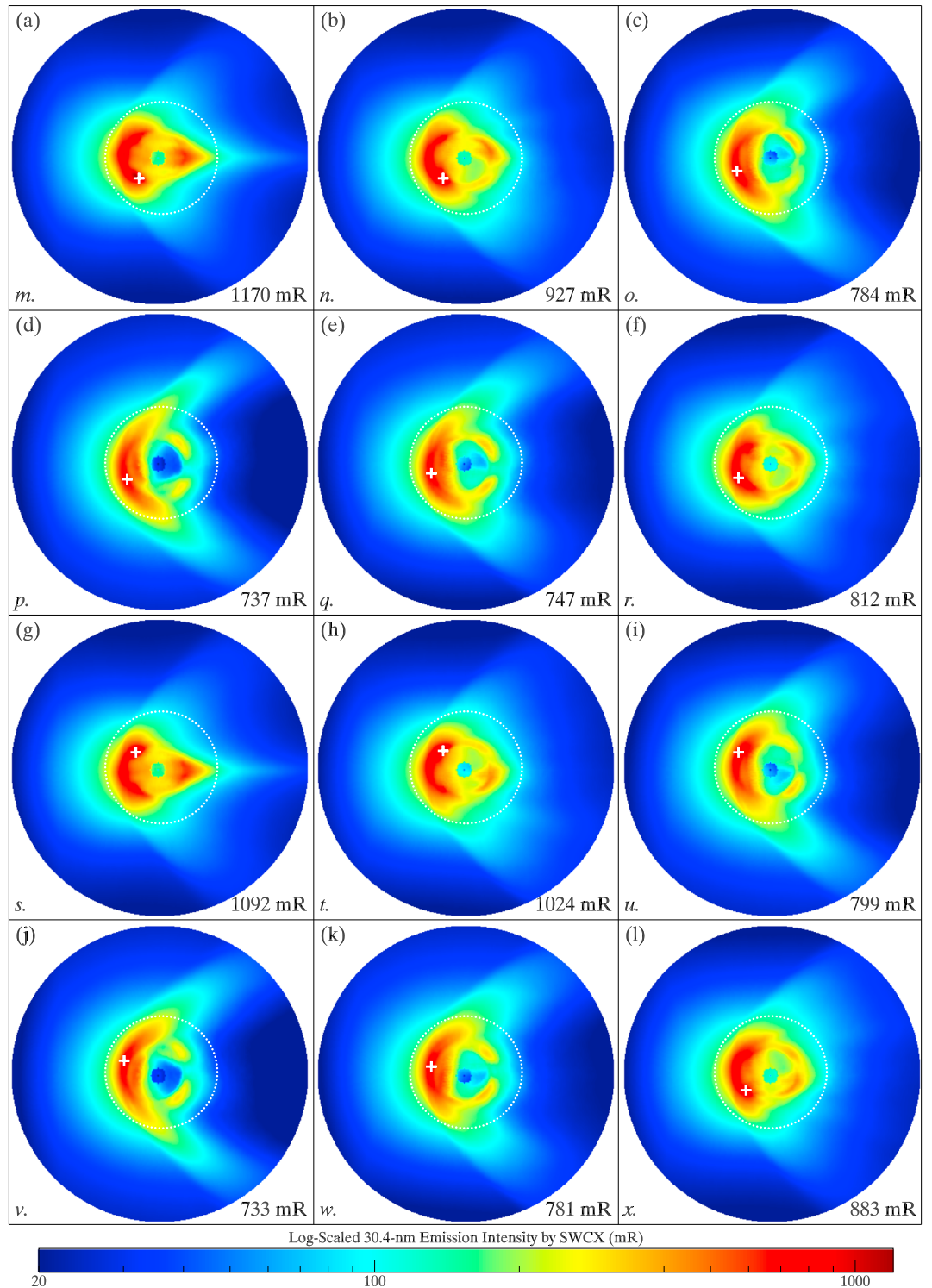Log-Scaled 30.4-nm Emission Intensity by SWCX (mR)

Figure 16. Magnetosheath EUV emission intensity simulated at the 12 positions in Figure 4. Each box represents a position in Figure 4 as indicated at the lower left corner of each box. The projection plane for all the boxes are the SCS yz plane, the Y_{SCS} axis (also the X_{GSM} axis) is in horizontal direction with positive to the left and the Z_{SCS} axis is along the vertical direction with positive to the up. All the other settings are the same as those in Figure 5.
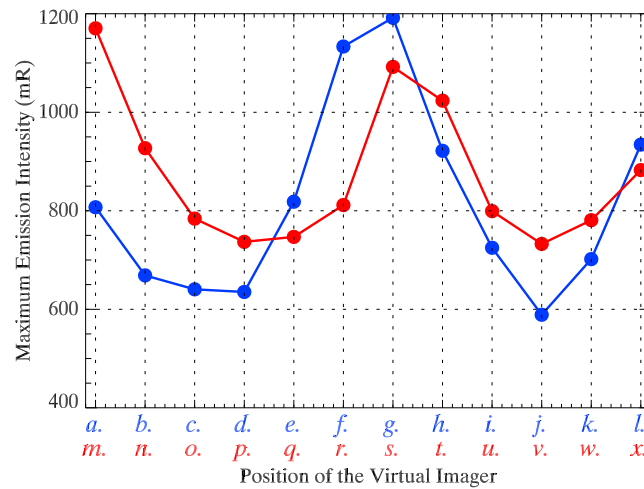
Figure 17. Maximum intensity simulated at positions a–x in Figure 4 with all inputs fixed with $V_{sw} = 700$ km/s, $N_{sw} = 40$ cm^{-3}, $T_{sw} = 50$ eV, $B_T = 25$ nT, $\theta_c = 180°$, and $f_\alpha = 0.2$.

3.3. Dependence of Emissions on f_α

The dependences of the magnetosheath EUV emission intensity distributions and the maximum emission intensities on f_α are shown in Figure 13 (category VI) and Figure 14, respectively, with all other parameters fixed with $V_{sw} = 500$ km/s, $N_{sw} = 10$ cm^{-3}, $T_{sw} = 20$ eV, $B_T = 10$ nT, and $\theta_c = 180°$. Noting that f_α is typically ~0.05 for general solar wind conditions [*Kivelson and Russell*, 1995], but it can reach 0.2 ~ 0.4 for extreme solar wind conditions (typically for coronal mass ejections, CMEs) [*Skoug et al.*, 2004]. It can be seen in Figures 13, 14 that the overall emission intensities in the magnetosphere increase almost linearly with f_α resulting from the increase of n_α, associated with little change in the intensity distribution pattern.

3.4. Intensity Distributions at Different Imaging Positions

In order to better understand the effect of different imaging perspectives on the magnetosheath EUV emission intensities, images simulated at all positions in Figure 4 are shown in Figures 15 and 16 (category VII) with all inputs fixed with $V_{sw} = 700$ km/s, $N_{sw} = 40$ cm^{-3}, $T_{sw} = 50$ eV, $B_T = 25$ nT, $\theta_c = 180°$, and $f_\alpha = 0.2$. It is noted that the SWCX EUV emissions in the magnetosheath can be as high as ~1200 mR if the virtual imager is in the first-quarter Moon (Figures 15f, 15g, and 16a) or the last-quarter Moon (Figures 15a, 15l, and 16g) as also shown in Figure 17. The intensity peaks appear at positions a,g, m, and s near the dawn-dusk line, and the intensity valleys appear at positions d, j, p, and v near the noon-midnight line or the Earth's magnetic pole, with a peak-to-valley ratio of ~2.0 as shown in Figure 17. It is also inferred in Figures 15, 16 that the EUV emission patterns simulated at different positions are significantly different and reflect different latitudinal and longitudinal information of the magnetosheath and the nightside ring current region.

4. Summary and Conclusion

In this paper, a 3-D global hybrid simulation code and a 3-D geocoronal hydrogen model are used to systematically study the 30.4 nm emissions in the SWCX process in the Earth's magnetosheath, associated with different SW-IMF conditions and different imaging perspectives. The main results are summarized as follows.

1. The intensities of the SWCX EUV emissions in the magnetosheath are highly variable from several mR for quiet SW-IMF conditions to ~1200 mR for disturbed SW-IMF conditions. It is noted in this investigation that the SW-IMF conditions in Table 1 are used to drive the 3-D global hybrid simulation code to produce the realistic configurations of the magnetosphere [*Lin and Wang*, 2005; *Lin et al.*, 2014]. However, for extremely high speed solar wind conditions, P_d and MA may enhance to ~100 nPa and ~20 [*Skoug et al.*, 2004] for which the simulation code might not produce reasonable magnetospheric configurations [*Lin et al.*, 2014], and the emission intensity in the magnetosheath might be significantly greater than 1200 mR. Considering seasonal and solar cycle variations for the *Hodges* [1994] model, n_H at solstice is ~1.25 times of equinox, and n_H for solar minimum is ~1.33 times of solar maximum in the magnetosheath region, respectively. For fixed SW-IMF conditions the SWCX emission intensities at solstice for solar maximum, at equinox for solar minimum, and at solstice for solar minimum can be approximately estimated by multiplying 1.25, 1.33, and 1.67, respectively.

2. It is found that θ_c, B_T, V_{sw}, N_{sw}, and f_α are important parameters to control the SWCX EUV emission patterns in the magnetosheath and T_{sw} plays less important role. Southward IMF and small B_T produce more intense emissions compared with northward IMF and large B_T, and the emission patterns may be complex and highly variable during disturbed IMF conditions. The SWCX EUV emissions in the magnetosheath quadratically intensify with the increase of V_{sw} due to the enhancements in u_α and $\sigma_{30.4}$, and with the increase of N_{sw} resulting from the enhancement in n_α, respectively, resulted from the fact that an increase in P_d compresses the magnetosheath close to the Earth, allowing more solar wind alpha particles to enter the magnetosheath in which n_H is higher. It can be seen that the SWCX EUV emission intensity in the magnetosheath increases linearly with f_α but does not vary much with T_{sw}, possibly due to the fact that the kinetic energy is much larger than the thermal energy in the solar wind.

3. It is revealed that the SWCX EUV emission intensities in the magnetosheath highly depend on the imaging positions and the simulated EUV images at different imaging perspectives can reflect different latitudinal and longitudinal information of the magnetosheath and the nightside ring current region. The simulation results indicate that the SWCX EUV emission intensities in the magnetosheath can be as high as ~1200 mR if the virtual imager is near the dawn-dusk line and as low as ~600 mR if it is near the noon-midnight line or the Earth's magnetic pole. It is suggested that, imaging at dawn or dusk on magnetic equatorial plane can reveal the latitudinal configurations of the bow shock, the magnetopause, the magnetosheath and the cusps in the magnetosphere, and imaging from the polar region can capture the longitudinal configurations of those structures. Of course, combined imaging from both equatorial and polar perspectives can obtain the three-dimensional structures of the magnetosphere.

4. The EUV emissions produced in the SWCX process in the magnetosheath for disturbed solar wind conditions could achieve or exceed 100 mR, the threshold of current remote sensing EUV imagers [*Sandel et al.*, 2000; *He et al.*, 2013; *Chen et al.*, 2014], near the plasmapause. Therefore, the SWCX EUV emissions in the magnetosheath for highly disturbed SW-IMF conditions should be taken into consideration in processing the Moon-based plasmaspheric EUV images and image inversions.

5. It can be inferred from the simulations and above discussions that, EUV imaging of the global magnetosheath under different SW-IMF conditions requires an EUV imager with large FOV, high-sensitivity, large dynamic range, and low intrinsic dark count rate. Considering a EUV imager 60 R_E away from the Earth's center, we suggest that a FOV of 40° with angular resolution of 0.2° should be suitable for imaging the global magnetosheath in one snapshot, the dynamic range of the camera should achieve at least 10^4 to cover the target intensity from ~10 mR to ~10 R (including the plasmasphere), the intrinsic dark count rate for a microchannel plate detector should be less than 1 count $cm^{-2} s^{-1}$, and the sensitivity should be as high as possible for better quality of the images.

It is known that the sensitivity (S) is a key parameter to determine the signal-to-noise ratio (SNR) of the images and $S = 10^6 \times A_e \times \omega \times \rho \times \tau \times \varepsilon/(4\pi)$, where A_e is the area of the entrance aperture, ω is the solid angle of the angular resolution, ρ is the reflectivity of mirror, τ is the filter transmission, and ε is the quantum efficiency of the detector. Generally, S can also be expressed in the form of $S = SNR^2 \times (I_s + 2I_b)/(I_s^2 \times T)$, where I_s, I_b, and T are the target intensity, the background intensities, and the exposure time, respectively.

Only two sources for I_b are considered in the magnetosheath imaging, one is the interplanetary 30.4 nm background which is averagely ~2 mR [*Gruntman*, 2001], and the other one is the interplanetary 58.4 nm background which is ~1.5 mR [*Wu et al.*, 1981; *Jelinsky et al.*, 1995] (using attenuation relative to 30.4 nm of ~1000 for the filter transmission, detector efficiency, and multilayer mirror reflectivity [*Davis et al.*, 2013]). Thus, I_b is ~3.5 mR for the magnetosheath imaging.

According to currently realizable technique levels of EUV imagers [*Davis et al.*, 2013; *Chen et al.*, 2014], $A_e = 80$ cm^2, $\omega = 1.22 \times 10^{-5}$ sr (corresponds to 0.2 R_E spatial resolution), $\rho = 0.4$, $\tau = 0.3$, and $\varepsilon = 0.15$, and S can achieve ~1.6 count s^{-1} R^{-1} pixel^{-1}. For a target intensity of $I_s = 10$ mR, in order to get a SNR of 3 (commonly accepted SNR level), the exposure time should be at least 1080 s. If the imager-to-Earth distance is reduced to 40 R_E, ω can be enlarged to 2.74×10^{-5} sr for the same spatial resolution (or increase A_e to 180 cm^2, but

the imager can be very large and may be not achievable), then S can achieve ~3.6 count s^{-1} R^{-1} pixel^{-1}, and the corresponding exposure time can be less than 600 s, which is commonly accepted in current EUV imaging of geospace [*Sandel et al.*, 2000; *Chen et al.*, 2014]. It is suggested that, in order to realize better temporal resolution and spatial resolution for magnetosheath EUV imaging, the sensitivity should be as high as possible, but this depends on the development of EUV imagers and also depends on the imaging orbits [*Davis et al.*, 2013; *Gruntman*, 2008, and references therein].

This paper provides us with a clear overall understanding of the EUV emissions in the SWCX process in the Earth's magnetosheath for different SW-IMF conditions and different imaging perspectives. It is expected that well-designed EUV imager will be used to image the global magnetosheath to study the solar wind-magnetosphere coupling in the future.

References

Bailey, J., and M. Gruntman (2011), Experimental study of exospheric hydrogen atom distributions by Lyman-alpha detectors on the TWINS mission, *J. Geophys. Res.*, *116*, A09302, doi:10.1029/2011JA016531.

Bhardwaj, A., et al. (2002), Soft X-ray emissions from planets, Moons, and comets, in *Earth-Like Planets and Moons, Proceedings of the 36th ESLAB Symposium, Eur. Space Agency Spec. Publ., ESA SP-514,* edited by B. Foing and B. Battrick, pp. 215–226, ESTEC, Noordwijk, Netherlands.

Bishop, J. (1999), Transport of resonant atomic hydrogen emissions in the thermosphere and geocorona: Model description and applications, *J. Quant. Spectrosc. Radiat. Transfer*, *61*, 473–491.

Bodewits, D., R. Hoekstra, B. Seredyuk, R. W. McCullough, G. H. Jones, and A. G. G. M. Tielens (2006), Change exchange emission from solar wind helium ions, *Astrophys. J.*, *642*, 593–605.

Bothmer, V., and I. A. Daglis (2007), *Space Weather-Physics and Effects*, Springer, in association with Praxis Ltd, Chichester.

Chao, J. K., D. J. Wu, C.-H. Lin, Y. H. Yang, X. Y. Wang, M. Kessel, S. H. Chen, and R. P. Lepping (2002), Models for the size and shape of the Earth's magnetopause and bow shock, in *Space Weather Study Using Multipoint Techniques, COSPAR Colloq. Ser.*, vol. 12, edited by L.-H. Lyu, pp. 127–134, Pergamon, Oxford, U. K.

Chen, B., et al. (2014), Investigation and calibration of the Moon-based EUV camera for Chang'E-3, *Res. Astron. Astrophys.*, doi:10.1088/1674-4527/14/12/013.

Cravens, T. E. (1997), Comet Hyakutake X-ray source: Charge transfer of solar wind heavy ions, *Geophys. Res. Lett.*, *24*, 105–108, doi:10.1029/96GL03780.

Cravens, T. E. (2002), X-ray emission from comets, *Science*, *296*, 1042–1045.

Davis, M. W., G. R. Gladstone, J. Goldstein, B. R. Sandel, T. K. Greathouse, K. D. Retherford, and G. S. Winters (2013), An improved wide-field camera for imaging Earth's plasmasphere at 30.4 nm, *Proc. SPIE*, *8859*, 88590U, doi:10.1117/12.2024440.

Dennerl, K., J. Englhauser, and J. Trümper (1997), X-ray emissions from comets detected in the Röntgen X-ray satellite all-sky survey, *Science*, *277*, 1625–1630.

Ezoe, Y., et al. (2012), Suzaku observations of charge exchange emission from solar system objects, *Astron. Nachr.*, *333*(4), 319–323, doi:10.1002/asna.201211664.

Fujimoto, R., K. Mitsuda, D. McCammon, Y. Takei, M. Bauer, Y. Ishisaki, F. S. Porter, H. Yamaguchi, K. Hayashida, and N. Y. Yamasaki (2007), Evidence for solar wind charge-exchange X-ray emission from the Earth's magnetosheath, *Publ. Astron. Soc. Jpn.*, *59*, S133–S140.

Fuselier, S. A., et al. (2010), Energetic neutral atoms from the Earth's subsolar magnetopause, *Geophys. Res. Lett.*, *37*, L13101, doi:10.1029/2010GL044140.

Gruntman, M. (1992), Charge-exchange born He$^+$ ions in the solar wind, *Geophys. Res. Lett.*, *19*, 1323–1326, doi:10.1029/92GL01277.

Gruntman, M. (2001), Imaging the three-dimensional solar wind, *J. Geophys. Res.*, *106*(A5), 8205–8216, doi:10.1029/2000JA000277.

Gruntman, M. (2008), Exploring the solar system galactic frontier in extreme ultraviolet, *Acta Astronaut.*, *63*, 1203–1214.

Gruntman, M., V. Izmodenov, and V. Pizzo (2006), Imaging the global solar wind flow in EUV, *J. Geophys. Res.*, *111*, A04216, doi:10.1029/2005JA011530.

He, F., X.-X. Zhang, B. Chen, and M.-C. Fok (2011), Reconstruction of the plasmasphere from Moon-based EUV images, *J. Geophys. Res.*, *116*, A11203, doi:10.1029/2010JA016364.

He, F., X.-X. Zhang, B. Chen, M.-C. Fok, and Y.-L. Zou (2013), Moon-based EUV imaging of the Earth's Plasmasphere: Model simulations, *J. Geophys. Res. Space Physics*, *118*, 7085–7103, doi:10.1002/2013JA018962.

Hodges, R. R., Jr. (1994), Monte Carlo simulation of the terrestrial hydrogen exosphere, *J. Geophys. Res.*, *99*(A12), 23,229–23,247, doi:10.1029/94JA02183.

Jelinsky, P., J. V. Vallega, and J. Edelstein (1995), First spectral observations of the diffuse background with the Extreme Ultraviolet Explorer, *Astrophys. J.*, *442*, 653–661.

Kivelson, M. G., and C. T. Russell (1995), *Introduction to Space Physics*, Cambridge Univ. Press, Cambridge, U. K.

Krasnopolsky, V. A., J. B. Greenwood, and P. C. Stancil (2005), X-ray and extreme ultraviolet emissions from comets, *Space Sci. Rev.*, *113*, 271–373.

Lin, R. L., X. X. Zhang, S. Q. Liu, Y. L. Wang, and J. C. Gong (2010), A three-dimensional asymmetric magnetopause model, *J. Geophys. Res.*, *115*, A04207, doi:10.1029/2009JA014235.

Lin, Y., and X. Y. Wang (2005), Three-dimensional global hybrid simulation of dayside dynamics associated with the quasi-parallel bow shock, *J. Geophys. Res.*, *110*, A12216, doi:10.1029/2005JA011243.

Lin, Y., X. Y. Wang, S. Lu, J. D. Perez, and Q. Lu (2014), Investigation of storm-time magnetotail and ion injection using three-dimensional global hybrid simulation, *J. Geophys. Res. Space Physics*, *119*, 7413–7432, doi:10.1002/2014JA020005.

Lisse, C. M., D. J. Christian, K. Dennerl, K. J. Meech, R. Petre, H. A. Weaver, and S. J. Wolk (2001), Charge exchange-induced X-ray emission from comet C/1999 S4 (LINEAR), *Science*, *292*, 1343–1348, doi:10.1126/science.292.5520.1343.

Omidi, N., X. Blanco-Cano, and C. T. Russell (2005), Macrostructure of collisionless bow shock and ion foreshock: Scale lengths, *J. Geophys. Res.*, *110*, A12212, doi:10.1029/2005JA011169.

Østgaard, N., S. B. Mende, H. U. Frey, G. R. Gladstone, and H. Lauche (2003), Neutral hydrogen density profiles derived from geocoronal imaging, *J. Geophys. Res.*, *108*(A7), 1300, doi:10.1029/2002JA009749.

Paresce, F., H. Fahr, and G. Lay (1981), A search for interplanetary He II, 304-A emission, *J. Geophys. Res.*, *86*(A12), 10,038–10,048, doi:10.1029/JA086iA12p10038.

Raeder, J. (2003), Global magnetohydrodynamics—A tutorial, in *Space Plasma Simulation*, *Lecture Notes in Physics*, vol. 615, edited by J. Büchner, C. T. Dum, and M. Scholer, pp. 212–246, Springer, Berlin, doi:10.1007/3-540-36530-3_11.

Rairden, R. L., L. A. Frank, and J. D. Craven (1986), Geocoronal imaging with dynamics explorer, *J. Geophys. Res.*, *91*, 13,613–13,630, doi:10.1029/JA091iA12p13613.

Robertson, I. P., and T. E. Cravens (2003), X-ray emission from the terrestrial magnetosheath, *Geophys. Res. Lett.*, *30*(8), 1439, doi:10.1029/2002GL016740.

Robertson, I. P., M. R. Collier, T. E. Cravens, and M. -C. Fok (2006), X-ray emission from the terrestrial magnetosheath including the cusps, *J. Geophys. Res.*, *111*, A12105, doi:10.1029/2006JA011672.

Sandel, B. R., et al. (2000), The extreme ultraviolet imager investigation for the image mission, *Space Sci. Rev.*, *91*(1), 197–242.

Shue, J.-H., et al. (1998), Magnetopause location under extreme solar wind conditions, *J. Geophys. Res.*, *103*(A8), 17,691–17,700, doi:10.1029/98JA01103.

Skoug, R. M., J. T. Gosling, J. T. Steinberg, D. J. McComas, C. W. Smith, N. F. Ness, Q. Hu, and L. F. Burlaga (2004), Extremely high speed solar wind: 29–30 October 2003, *J. Geophys. Res.*, *109*, A09102, doi:10.1029/2004JA010494.

Swift, D. W. (1996), Use of a hybrid code for a global-scale plasma simulation, *J. Comput. Phys.*, *126*, 109–121.

Tan, B., Y. Lin, J. D. Perez, and X. Y. Wang (2011), Global-scale hybrid simulation of dayside magnetic reconnection under southward IMF: Structure and evolution of reconnection, *J. Geophys. Res.*, *116*, A02206, doi:10.1029/2010JA015580.

Tinsley, B. A., R. R. Hodges Jr., and R. P. Rhorbaugh (1986), Monte Carlo models for the terrestrial exosphere over a solar cycle, *J. Geophys. Res.*, *91*, 13,631–13,647, doi:10.1029/JA091iA12p13631.

Wargelin, B. J., M. Markevitch, M. Juda, V. Kharchenko, R. Edgar, and A. Dalgarno (2004), CHANDRA observations of the "dark" Moon and geocoronal solar wind charge transfer, *Astrophys. J.*, *607*, 596–610.

Wu, F. M., K. Suzuki, R. W. Carlson, and D. L. Judge (1981), PIONEER 10 ultraviolet photometer observations of the interplanetary glow at heliocentric distances from 2 to 14 AU, *Astrophys. J.*, *245*, 1145–1158.